

Staggered Dzyaloshinskii-Moriya and canting angle in centrosymmetric altermagnetic and ferromagnetic phases: influence on the anomalous Hall effect and Weyl points

Mathews Benny , ^{1,*} Xujia Gong , ¹ Kamil Jamroscopiczky, ¹ Amar Fakhredine , ² Giuseppe Cuono , ^{3,4} Rajibul Islam , ⁵ Jan Skolimowski , ^{1,†} and Carmine Autieri , ^{1,6,‡}

¹*International Research Centre Magtop, Institute of Physics,*

Polish Academy of Sciences, Aleja Lotników 32/46, PL-02668 Warsaw, Poland

²*Institute of Physics, Polish Academy of Sciences, Aleja Lotników 32/46, 02668 Warsaw, Poland*

³*Department of Materials Science, University of Milan-Bicocca, Via Roberto Cozzi 55, 20125 Milan, Italy*

⁴*Consiglio Nazionale delle Ricerche (CNR-SPIN),*

Unità di Ricerca presso Terzi c/o Università “G. D’Annunzio”, 66100 Chieti, Italy

⁵*Lomare Technologies Limited London Street, London EC3R 7LP, UK*

⁶*SPIN-CNR, UOS Salerno, IT-84084 Fisciano (SA), Italy*

(Dated: February 12, 2026)

We present a simple methodology to compute the anomalous Hall conductivity (AHC) as a function of the canting angles in ferromagnets and altermagnets, starting from a nonmagnetic Hamiltonian obtained from first-principles calculations that preserves the full symmetry of the crystal structure. Magnetism is introduced by including on-site spin splitting, spin-orbit coupling, and spin-canting angles. As a representative material, we study SrRuO_3 , which supports spin canting and exhibits a sign change of the AHC. In the ferromagnetic phase, the low-energy AHC is found to be close to zero at the Fermi level, in agreement with experimental observations. We show that the dependence of the AHC on the relevant physical parameters is most pronounced in the central region of the electronic bandwidth. We determine the symmetry-allowed components of the AHC for different magnetic orders in the large family of transition-metal perovskite ABO_3 compounds with space group 62, including the spontaneous in-plane anomalous Hall effect. Within density functional theory, we evaluate the range of spin-canting angles in SrRuO_3 and demonstrate that it is suppressed as electronic correlations increase. By analyzing the AHC as a function of the canting angle, we find that the collinear magnetic configurations contribute most to the AHC, while spin canting plays a secondary role in determining its magnitude in non-collinear ferromagnets and altermagnets. However, canting can become relevant and induce a sign change of the AHC when the collinear magnetic state exhibits an AHC close to zero. Finally, we investigate the locations of Weyl points in the Brillouin zone and their evolution as a function of the canting angle.

I. INTRODUCTION

Over the past decades, significant effort has been devoted to understanding the effects of a net Dzyaloshinskii-Moriya interaction (DMI) on the magnetotransport properties of magnetic materials, since it promotes spin canting and can lead to the formation of chiral magnetic textures such as skyrmions, especially in ferromagnetic systems^{1–4}. On the other hand, researchers have investigated the effect of *staggered* DMI in altermagnets^{5,6}. DMI is a relativistic, antisymmetric component of the exchange interaction arising from first-order in the spin-orbit coupling (SOC). SOC preserves time-reversal symmetry and therefore is unable to generate magnetism or weak ferromagnetism in systems with Kramers degeneracy. Consequently, in centrosymmetric and time-reversal-symmetric systems, SOC alone is insufficient to lift spin degeneracy or induce a net magnetic moment. In altermagnetic compounds, however, time-reversal symmetry is broken while the net magnetization remains zero in the non-relativistic limit^{7,8}. In this case, the presence of an altermagnetic spin splitting allows SOC to generate a finite weak ferromagnetic moment. The altermagnetic spin-splitting is therefore a necessary condition for the emergence of weak ferro-

magnetism in centrosymmetric systems. However, also higher orders in SOC with a behavior similar to the DMI can produce weak ferromagnetism^{5,9}. When weak ferromagnetism is symmetry-allowed, the anomalous Hall conductivity (AHC) is likewise symmetry-allowed^{10,11}. The AHC effect can be further enhanced by the presence of Weyl points near the Fermi energy¹². The orientation of the Hall vector is strongly dependent on the Néel vector, which is defined as the difference between the magnetization vectors of the two inequivalent magnetic sublattices^{13,14}. It has been predicted that the anomalous Hall response can also serve as a sensitive probe of the Néel vector^{15,16}. Recently, the link between anomalous Hall conductivity and Fermi surface geometry has been emphasized¹⁷. A more general discussion of the symmetry-allowed terms obtained from a multipole analysis was done for the anomalous and planar Hall effect^{18,19}.

In contrast, much less attention has been paid to the role of a *staggered* DMI in ferromagnetic systems that preserve inversion symmetry²⁰. The staggered DMI is absent in PT-symmetric systems, but it induces spin canting in both altermagnets and ferromagnets. While the staggered DMI tends to generate weak ferromagnetism in altermagnets, it tends to generate spin canting in fer-

romagnets, which, in the simplest cases, gives a zero net magnetization along the subdominant components²¹. The effect of the staggered DMI in real materials on the magnetic, transport and topological properties is usually neglected.

Members of the Ruddlesden–Popper series of Sr-ruthenate oxides^{22,23}, and more generally transition-metal oxides²⁴, host rotational symmetries that generate staggered DMI. These same symmetries can also give rise to altermagnetism in systems with antiferromagnetic interactions. Consequently, transition-metal-oxide perovskites represent an extraordinary platform for realizing altermagnetic materials^{23,25,26}. SrRuO₃ is one of the most extensively studied itinerant ferromagnetic oxides²⁷, owing to the wide tunability of its properties in thin films²⁸ and at interfaces^{29–34}. This tunability has enabled applications in quantum electronics³⁵, free-standing membranes³⁶, and the investigation of curvilinear magnetism³⁷. Using first-principles methods, several studies have explored the effects of strain^{38,39}, electronic correlations⁴⁰, reduced dimensionality^{41–43}, and heterostructuring^{44,45} on the electronic and magnetic properties of SrRuO₃. More recently, this material has also been proposed to host an unconventional orbital Hall effect⁴⁶. The presence of spin canting in SrRuO₃ was demonstrated using first-principles calculations⁴⁷, and its impact on the anomalous Hall effect was subsequently analyzed in terms of chirality for the antiferromagnetic single layer of SrRuO₃⁴⁸. Recently, we reported relativistic spin-momentum locking in the ferromagnetic phases of SrRuO₃. For the ferromagnetic phase of SrRuO₃ with magnetization along the z axis, the relativistic spin-momentum locking consists of d -wave magnetism, characterized by the magnetic quadrupoles Q_{xz} and Q_{yz} , in the subdominant spin components S_x and S_y respectively. The dominant component S_z has been shown to exhibit s -wave magnetism.⁴⁹ In (111)-orientated SrRuO₃, recent studies revealed that a component of the AHC was observed in the same direction as the dominant component⁵⁰, highlighting the important role of subdominant components in the AHC of ferromagnets.

The AHC of SrRuO₃ has been shown to undergo a sign reversal when interfaced with materials possessing strong spin-orbit coupling, or when magnetism is perturbed at the interface or the surface^{29–34}. Theoretically, it has been demonstrated that even in the absence of staggered DMI, the spin canting alone can induce a sign change in the Berry curvature and consequently in the AHC⁵¹. Furthermore, the sign of the AHC can be directly related to differences in the orbital angular momentum⁵².

In this work, we aim to establish a general framework for calculating the anomalous Hall conductivity in collinear magnetic phases of transition-metal perovskites and to investigate the influence of staggered DMI on both the AHC and on the Weyl points. The paper is organized as follows. Section 2 presents the methodology used to construct the magnetic Hamiltonian via Wannierization of nonmagnetic first-principles calculations, which pre-

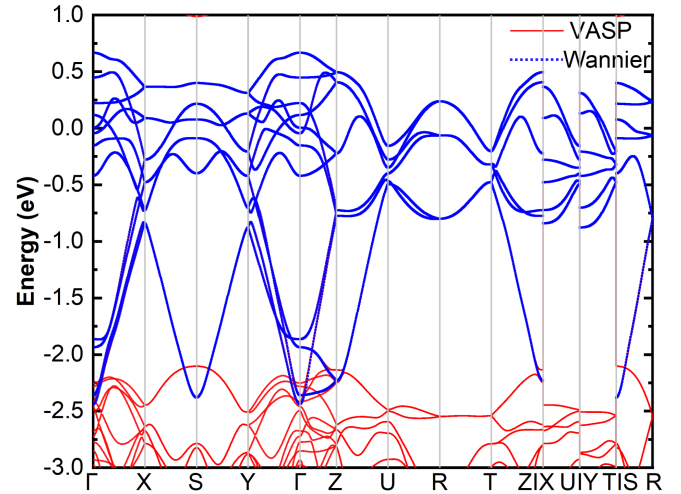


FIG. 1. Comparison of the non-magnetic electronic band structures obtained from Wannier interpolation (blue dotted lines) and DFT calculations performed using the VASP code (red lines). The Wannier basis set was constructed using the t_{2g} orbitals as trial wave functions. The Wannier-interpolated bands are in excellent agreement with the direct DFT results across the entire Brillouin zone.

serves the crystal symmetries with high fidelity. Section 3 reports the AHC for all magnetic orders of the perovskite ABO₃ and analyzes their associated symmetries. In Section 4, we report the magnitude of the spin cantings and the sign reversal of the AHC; therefore, we analyze the evolution of the Weyl-point trajectories as a function of the staggered DMI. Finally, Section 6 summarizes the main conclusions of this work.

II. BAND STRUCTURE CALCULATION AND TIGHT-BINDING MODEL IN NON-MAGNETIC PHASE

Performing AHC calculations using density functional theory (DFT) calculations within a relativistic framework presents two major challenges. First, the inclusion of SOC constrains the spin orientation to the underlying crystal symmetry, making it generally impossible to tune the canting angles. This limitation complicates the study of systems where non-collinear spin configurations or weak ferromagnetism play a significant role. Second, while the Wannierization of relativistic band structures is used in the standard procedure⁵³, it is often a nontrivial task, especially for large systems or complex magnetic phases. The construction of maximally localized Wannier functions (MLWFs) in the presence of SOC often yields non-symmetrized tight-binding Hamiltonians, even when the procedure is carefully optimized. Although several computational packages offer Hamiltonian symmetrization routines, these implementations typically apply only to non-relativistic cases.

To overcome both of these issues, we adopt an alterna-

tive procedure. In order to tune the canting angles while preserving all symmetries of the Hamiltonian, we start from the non-magnetic (NM) Hamiltonian constructed in the Wannier-function basis. This step is generally technically simpler, as the NM Hamiltonian involves a single spin channel, which is more easily disentangled. By contrast, in the magnetic cases, the spin-splitting separates the bands into majority and minority components, increasing the likelihood of overlap with other non-magnetic bands. The non-magnetic Hamiltonian can be written in second quantization as:

$$H_{NM} = \sum_{i,j} t_{i,j}^{l,m} c_{i,l}^\dagger c_{j,m} \quad (1)$$

where i and j are the indexes for the atomic sites, while l and m run over the Wannier basis. The non-magnetic Hamiltonian, constructed in this way, already includes the crystal symmetries of the space group of the compounds, encompassing those symmetries that are responsible for altermagnetism. Once the local spin-splitting is added, the altermagnetic spin-splitting will appear. We add the on-site terms as the on-site spin-splitting $\vec{h}(\theta_S, \phi_S)$ dependent on the canting angles in polar coordinates and the SOC parameter λ , which is site-dependent when there is more than one atomic species. θ_S and ϕ_S are the polar and azimuthal angles of the given spin. Therefore, the additional terms of the Hamiltonian read:

$$H_{split} + H_{SOC} = \sum_i (-\vec{h}(\theta_S, \phi_S)_i \cdot \vec{S}_i + \lambda_i \vec{L}_i \cdot \vec{S}_i) \quad (2)$$

The module of the on-site spin-splitting can be tuned and the code provides a subroutine to renormalize the Fermi level for every value of the atom-dependent input parameters. The crucial information regarding the spin evolution is included in the real space magnetic configuration \vec{S}_i and their angular dependence can be obtained by symmetry analysis or by studying the relativistic spin-resolved density of states (DOS)^{6,54}. The ferromagnetic configuration with spins along the z-axis is achieved by setting $\theta_S = \phi_S = 0$ for all magnetic atoms and so on for all other magnetic configurations. The implementation code for this research is publicly available as open-source software⁵⁵. The code can be used to generate spin cantings for p, d, and f electrons on top of the non-magnetic Hamiltonian, ensuring that the final Hamiltonian possesses the correct magnetic symmetries. This code that incorporates the accuracy of first-principles and the crystal symmetries could be applied, for instance, to study magnetic multipoles⁵⁶, non-collinear magnetic systems with commensurate magnetism⁵⁷, non-linear Hall effect¹⁶ and magnetic topological systems^{58,59}.

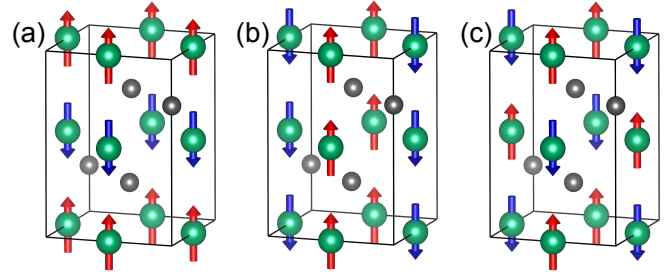


FIG. 2. The altermagnetic phases of SrRuO₃. (a) A-type magnetic order, (b) C-type magnetic order, and (c) G-type magnetic order. The Néel vector is aligned along the z-axis in all three cases.

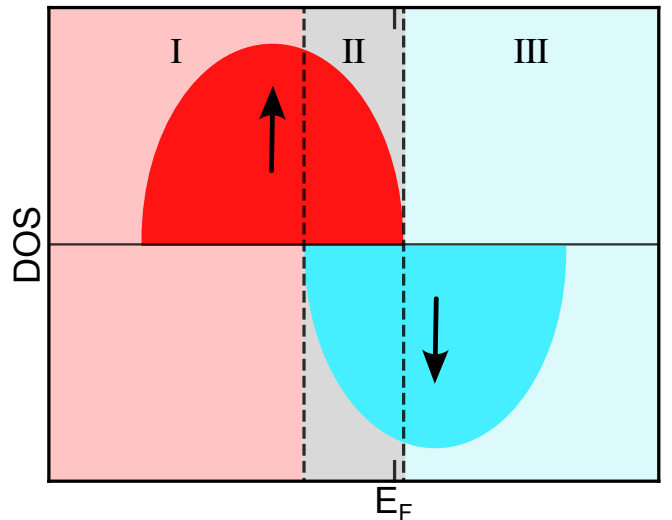


FIG. 3. A depiction of the three regions observed in the band structure in which the variation of AHC with spin-splitting has considerably different behaviour. The bright red (bright blue) region denotes the DOS of spin-up (down) electrons. The three regions of the AHC, at the bottom of the bands, around the Fermi level and above the Fermi level are represented in light red, light grey and light blue, respectively. In SrRuO₃, the t_{2g} manifold is filled to two-thirds (2/3).

A previous version of this code was used to describe the spin-canting in EuIn₂As₂⁶⁰. For the present paper, the non-magnetic band structure of SrRuO₃ is represented in Fig. 1 with the computational details reported in Appendix A. We have wannierized the t_{2g} electron bands; therefore, only Ru atoms are involved and we fix the spin-orbit to $\lambda_{Ru}=100$ meV. The value of 100 meV was extracted from the wannierization performed on the relativistic Hamiltonian and it agrees with previous literature⁶¹. The spin splitting of ferromagnetic SrRuO₃ was found to be around 1 eV within Local Spin Density Approximation, as determined from the difference between the spin-up and spin-down peaks in the DOS⁴². In this paper, we will analyze the effect of the spin-splitting in the range between 0.5 and 2.0 eV. Due to the properties of the crystal space group, the non-

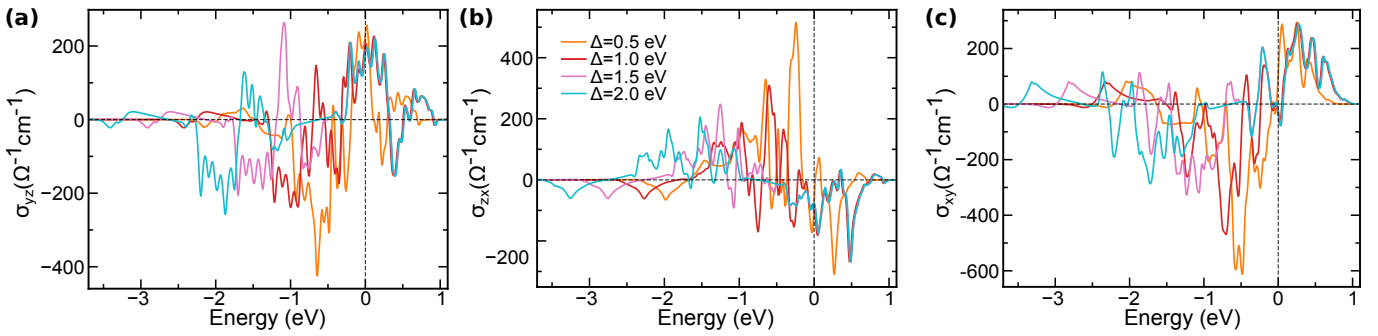


FIG. 4. AHC as a function of the spin splitting for the ferromagnetic phase with magnetization along the (a,b) x -direction with two non-zero components: σ_{yz} and σ_{zx} respectively. The first is the standard AHC, while the second is the spontaneous in-plane AHC. (c) z -direction where the only non-zero component is σ_{xy} .

collinear magnetic configuration of the 4 magnetic atoms depends only on two canting parameters that, from now on, we will define as θ and ϕ and their physical interpretation will be given later in the paper. The parameters Δ , θ , and ϕ were tuned within a realistic energy range, and the angles were chosen in accordance with the system's symmetry.

III. ANOMALOUS HALL EFFECT FOR THE DIFFERENT MAGNETIC PHASES AS A FUNCTION OF THE SPIN-SPLITTING

This section presents calculations of the AHC for different collinear magnetic phases as a function of the spin splitting, varied from 0.5 to 2.0 eV. We constrain these magnetic phases to be collinear, while most of them would become non-collinear after energy minimization when relativistic effects are included. All reported AHCS are spontaneous and do not require an external magnetic field. The aforementioned code⁵⁵ has been utilised to simulate the different collinear magnetic phases and values of the spin-splitting (Δ) on top of the NM Hamiltonian. These magnetic phases include the ferromagnetic phase and three collinear altermagnetic phases depicted in Fig. 2(a-c) with zero net magnetic moment. It has already been shown that the different magnetic orders in perovskite ABO_3 compounds are altermagnetic⁶²; however, the properties of the non-relativistic spin-momentum locking depend on the specific magnetic order²⁵.

A. Ferromagnetic order

We begin by simulating the AHC for the ferromagnetic phase with the magnetization along the x -, y -, and z -directions as a function of the on-site spin splitting Δ . For the ferromagnetic phase, the AHC can be qualitatively divided into three main energy regions: one above the Fermi level, one at the bottom of the bands, and one in the vicinity of the Fermi level. These three regions

are schematically represented in Fig. 3. Region I consists only of the majority states. Region II contains both majority and minority bands, while Region III consists only of minority states and can be assumed to behave similarly to Region I.

When the magnetization is along the x -axis, there are two contributions in the AHC tensor, namely σ_{yz} and σ_{zx} , which are reported in Fig. 4(a,b), respectively. Within DFT, we have tested the spin canting properties when the magnetization is along the x -axis and we found that the spins cant along the y -axis with two different magnitudes, resulting in a net magnetization along the y -axis, characteristic of a weak ferrimagnetism. This net magnetization along the subdominant component produces an additional spontaneous AHC component, which is less common and is the magnetic analogue to the in-plane Hall effect⁶³. Therefore, the component of the AHC can be identified as a spontaneous in-plane AHC described also for other ferromagnetic compounds^{18,64,65} and for altermagnets⁶⁶. The spontaneous in-plane anomalous Hall response was investigated in SrRuO_3 ⁵⁰, but for the (111) films, which have hexagonal symmetry. The AHC exhibits a pronounced dependence on the spin splitting. As the spin splitting increases, the electronic bandwidth of the system broadens, and the AHC spans a wider energy range, particularly as states below the Fermi level are pushed further away from it. In region I, the AHC peak shifts with increasing spin splitting; with the increasing of the spin splitting, the peak progressively moves away from the Fermi level. In region III, the AHC becomes independent of the spin splitting for $\Delta \geq 1.0$ eV. Region II corresponds to the crossing of the spin-up and spin-down bands; this region is the most sensitive to the variations in the parameters and also coincides with the location of the Fermi level. We note that σ_{zx} , in this case, is always relatively large at the Fermi level with a value of $200 \Omega^{-1} \text{cm}^{-1}$. When the magnetization direction is rotated by 90 degrees in the xy plane, a symmetry relation is observed between the AHC along the x - and y -directions. In particular, we find that the σ_{zx} for the magnetization along the x -axis is opposite to σ_{zx} for the magnetization along the y -axis,

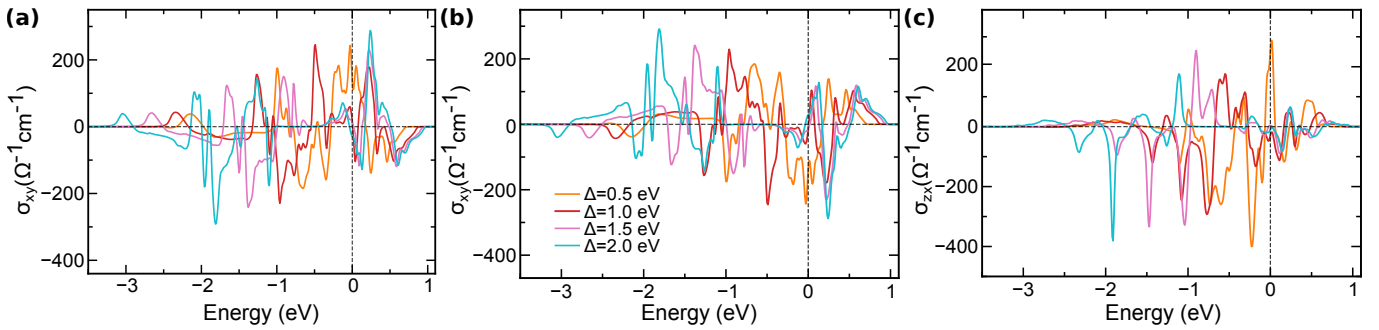


FIG. 5. AHC as a function of the spin splitting for the A-type altermagnet with Néel vector along the (a) x -direction, where the only nonzero component is σ_{xy} . (b) y -direction where the only nonzero component is σ_{xy} . (c) z -direction where the only nonzero component is σ_{zx} . All magnetic configurations are constrained to be collinear and exhibit zero net magnetization.

while the σ_{yz} for the magnetization along the x -axis is equal to σ_{yz} for the magnetization along the y -axis.

When the magnetization is along the z -axis, a non-zero AHC is observed in the σ_{xy} component, as shown in Fig. 4c, where it is plotted as a function of the on-site spin splitting Δ . Region III, above the Fermi level, is characterized by a positive AHC, which becomes independent of the spin splitting for $\Delta \geq 1.0$ eV. Region I is characterized by a negative AHC, while region II exhibits a small value, close to zero at the Fermi level. An AHC value close to zero would favor a sign change in the AHC, consistent with experimental observations.

B. Altermagnet with A-type magnetic order

The A-type altermagnetic phase was simulated with the Néel vector oriented along the x -, y -, and z -directions. Although weak ferromagnetism is symmetry-allowed and energetically favorable, it is explicitly constrained to be strictly zero in our calculations. Despite this constraint, the symmetry that allows weak ferromagnetism also permits a finite anomalous Hall effect along the same direction. Accordingly, a nonzero component of the AHC is obtained for all three orientations of the Néel vector.

For the A-type altermagnet with the Néel vector along the z -axis, the σ_{zx} component of AHC is non-zero, depicted in Fig. 5(c). For the other two cases, where the Néel vector is oriented along the x - and y -axes, respectively, the non-zero component of the AHC is σ_{xy} in both configurations as shown in Fig. 5(a) and Fig. 5(b). Moreover, the AHCs in the latter two cases are the exact opposite of each other. This relation should be present due to the symmetry of the conductivity tensor⁶⁷. The division into three regions that was schematically reported for the ferromagnetic phase persists slightly also in the altermagnetic phase, since it is easier to have anticrossing gaps in the middle of the bandwidth due to a larger number of bands. The quantity σ_{xy} for these magnetic phases can reach values of $\pm 200 \Omega^{-1} \text{cm}^{-1}$ at the Fermi level for $\Delta = 0.5$ eV.

For the altermagnetic phases, if we consider the intrin-

sic anomalous Hall resistivity ρ_{xy} without the effect of the magnetic domains, the phenomenological formula for the anomalous Hall resistivity⁶⁸ is not valid:

$$\rho_{xy} \neq R_0 B_z + R_s \mu_0 M_z = 0 \quad (3)$$

since both the external magnetic field B_z and the net magnetization along the z -axis M_z are zero, while ρ_{xy} (proportional to σ_{xy}) is not zero. R_0 and μ_0 are constants described in the literature⁶⁸. The same is valid for the next cases that we will describe.

C. Altermagnet with C-type magnetic order

The C-type magnetic order reveals AHC contributions that are in stark contrast to those found in the other magnetic configurations. In particular, when the Néel vector is oriented along the z -direction, all components of the AHC vanish. Although time-reversal symmetry is broken in this case, the system realizes a pure altermagnetic state in which neither weak ferromagnetism nor any AHC components are symmetry allowed. This phase constitutes the only pure altermagnetic state; nevertheless, it exhibits spin canting after energy minimization. This behavior is confirmed by DFT calculations, which show that the net magnetization remains zero despite the presence of spin canting, as in Ca_2RuO_4 ⁶⁹. Spin canting is therefore an intrinsic property of this class of materials, ABO_3 compounds with space group 62, whereas it can be symmetry-forbidden in other classes of materials⁴⁹.

In contrast, when the Néel vector is aligned along either the x - or y -direction, two nonzero components of the AHC emerge, namely σ_{yz} and σ_{zx} , as shown in Fig. 6. The σ_{zx} components are identical for both orientations of the Néel vector along the x - and y -directions. On the other hand, σ_{yz} changes sign when the Néel vector is rotated from the x -axis to the y -axis. This behavior closely resembles that observed in the ferromagnetic cases with the magnetization oriented along the x - and y -directions. The presence of multiple nonzero AHC components indicates that weak ferromagnetism is symmetry allowed in

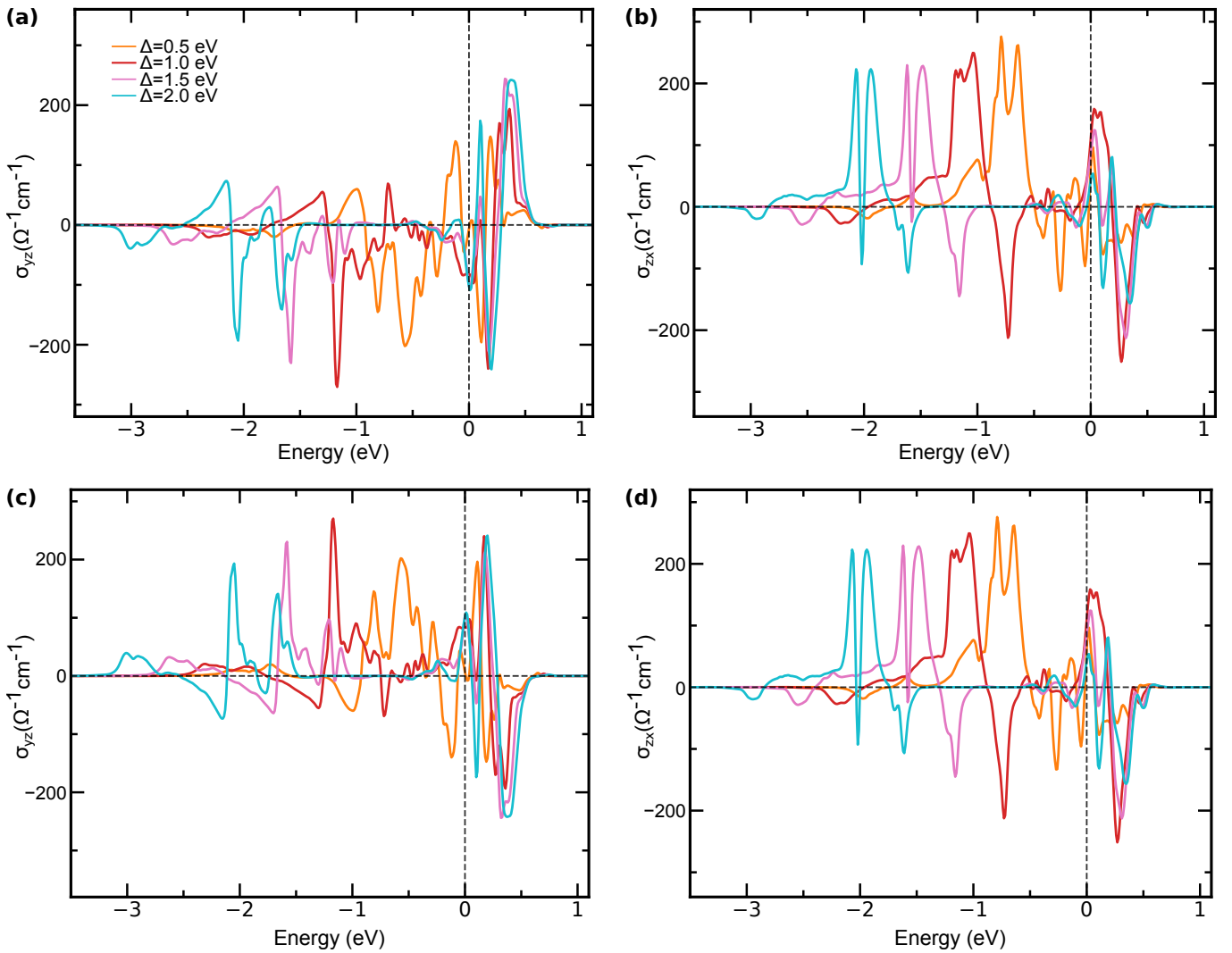


FIG. 6. AHC as a function of the spin splitting for the C-type altermagnet with Néel vector along the (a,b) x -direction with two non-zero components: σ_{yz} and σ_{zx} respectively, (c,d) y -direction where there are two non-zero component: (c) σ_{yz} and (d) σ_{zx} . All magnetic configurations are constrained to be collinear and exhibit zero net magnetization.

both configurations, consistent with our findings for the corresponding ferromagnetic states.

D. Altermagnet with G-type magnetic order

As for the A-type magnetic order, also in the case of G-type magnetic order, a nonzero component of the AHC is obtained when the Néel vector is oriented along all high-symmetry directions of the lattice vectors. The G-type magnetic order with the Néel vector oriented along the z -direction exhibits a non-zero component of the AHC, namely σ_{yz} , shown in Fig. 7c. When the Néel vector is oriented along the x - and y -directions, the σ_{xy} component of the AHC is non-zero. Moreover, the AHC is identical for both the latter cases. This can be observed in Fig. 7(a) and 7(b). We note that the same AHC component for the G-type magnetic order was calculated for

SrRuO₃ thin films⁷⁰.

We observe that, for the G-type magnetic order, the AHC reaches the largest absolute values with pronounced peaks close to the Fermi level of the order of about $450 \Omega^{-1}\text{cm}^{-1}$ when the Néel vector lies in the xy plane, and around $600 \Omega^{-1}\text{cm}^{-1}$ for the out of plane orientation. The latter in particular is comparable to the largest peak of the ferromagnetic phase in Fig. 4(c), and by far larger than the value of the ferromagnetic phase at the Fermi level.

We summarize our results for the anomalous Hall conductivity of SrRuO₃ in Table I. These results, obtained for SrRuO₃, rely crucially on the fact that it is an ABO₃ perovskite with space group no. 62, in which the magnetism resides on the B-site atoms. The same components of the anomalous Hall conductivity reported in Table I will be symmetry-allowed for systems of the same material class, such as vanadates^{25,71} and other oxides

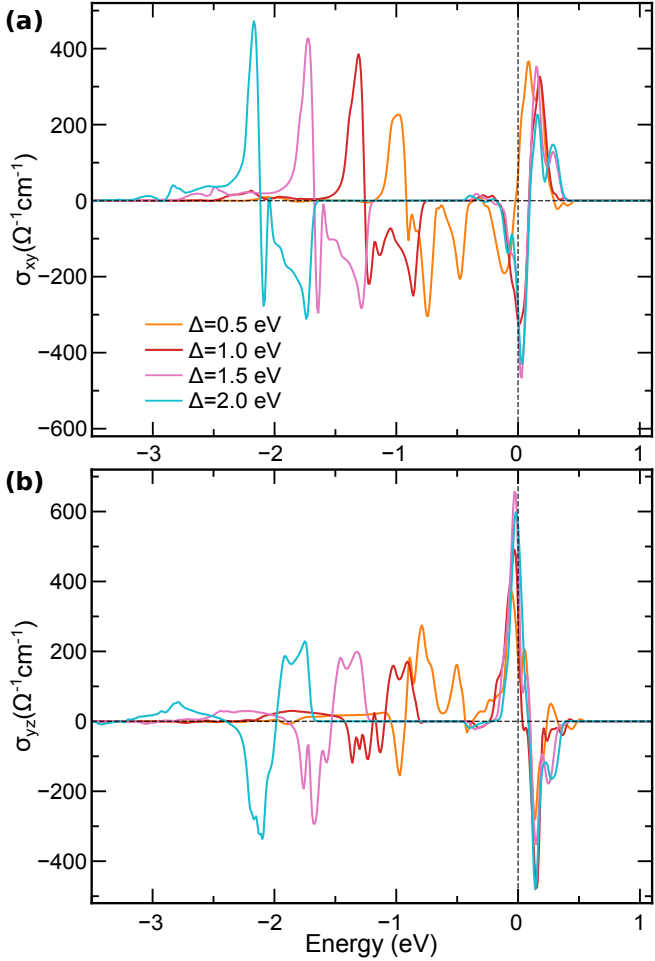


FIG. 7. AHC for the G-type magnetic order with (a) Néel vector along both the x - and the y -directions as a function of the spin-splitting. The only nonzero component is σ_{xy} for both cases. (b) Néel vector along the z -direction as a function of the spin-splitting. The only nonzero component is σ_{yz} . All magnetic configurations are constrained to be collinear and exhibit zero net magnetization.

Magnetic order	Only component of the Spin		
	S_x	S_y	S_z
Ferromagnet	σ_{yz}, σ_{zx}	σ_{yz}, σ_{zx}	σ_{xy}
A-type	σ_{xy}	σ_{xy}	σ_{zx}
C-type	σ_{yz}, σ_{zx}	σ_{yz}, σ_{zx}	Pure altermagnet
G-type	σ_{xy}	σ_{xy}	σ_{yz}

TABLE I. Spontaneous AHC for the different magnetic orders of the Pbnm crystal structure of the ABO_3 perovskite phase with B as magnetic atom. The spin has only one component, which is S_x , S_y or S_z , without spin-canting.

with the same space group⁷². The reported results show that for a given magnetic order, the same components of AHCs are allowed if the dominant component is along the S_x or S_y axis, while when the dominant component is along the S_z axis, the allowed AHCs always change with respect to the other direction. For the correspond-

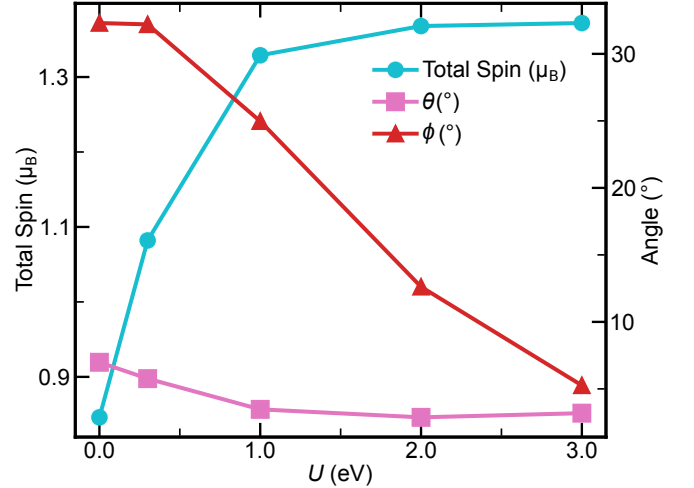


FIG. 8. Evolution of the total spin S , spin canting θ , and ϕ as a function of the Coulomb repulsion obtained within density functional theory.

ing orientation of the AHC, spin canting is symmetry allowed, and a weak ferromagnetic moment is therefore expected to emerge in DFT calculations, aligned with the AHC. In Table I, there is only one magnetic phase with pure altermagnetism. Moreover, we note that Table I contains several repeated entities. For instance, σ_{xy} appears 5 times while σ_{yz} in combination with σ_{zx} appears 4 times. This can be attributed to the magnetic space group and we will illustrate this for σ_{xy} in the next Section.

IV. AHC SIGN CHANGE AND WEYL POINT EVOLUTION IN THE FERROMAGNETIC PHASE WITH SPIN CANTING

We focus on the ferromagnetic phase with magnetization along the z -axis and we analyze the effect of the staggered DMI on the magnetic and transport properties. When SOC λ is included, the staggered DMI, which is linear in λ ⁷³, is implicitly taken into account. Spin canting, however, arises only after energy minimization, which can be obtained within first-principles calculations. In the first subsection, we describe and analyze the range of the canting angles obtained from first-principles calculations.

We proceed with the study of the influence of the spin canting on AHC, which has been performed only on the ferromagnetic phase with magnetization along the z -axis, since it is the experimental phase observed for bulk crystals. However, the same procedure could be applied for other magnetization directions and for the altermagnetic phases. For a realistic simulation of this compound, we will describe the behaviour of the spins S_i , S_h , S_j and S_k as a function of the canting angles. Since the canting angles depend on the staggered DMI parameters, by tuning the canting angles, we are manipulating the staggered DMI parameters. Therefore, the next subsections

will report the influence of the staggered DMI on the anomalous Hall effect and on the Weyl points.

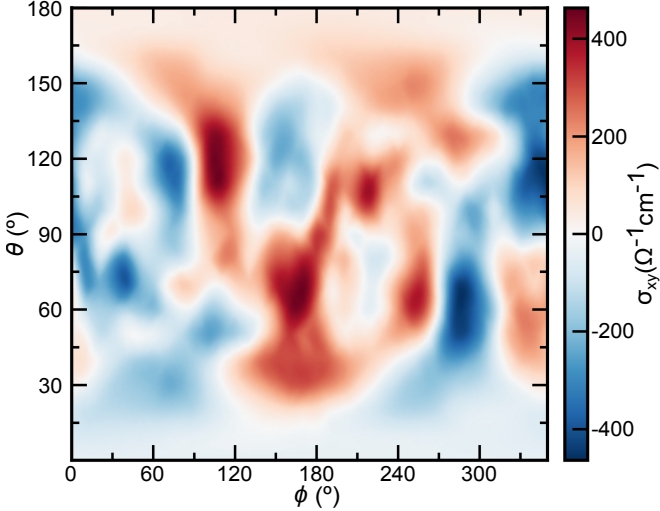


FIG. 9. The variation of the AHC, σ_{xy} , of the ferromagnetic phase at the Fermi level as a function of θ and ϕ . These data were generated for a spin-splitting of $\Delta=1$ eV.

A. Density functional theory for the ferromagnetic phase: θ and ϕ as a function of U

We perform DFT calculations for SrRuO_3 by using the computational setup described in Appendix A. Analyzing the DFT results, we observed that in the ferromagnetic phases, the four spins in the unit cell have canting angles and follow these equations:

$$S_h = (+S \sin(-\theta) \cos(-\phi), +S \sin(-\theta) \sin(-\phi), S \cos(\theta)) \quad (4)$$

$$S_i = (+S \sin(+\theta) \cos(+\phi), +S \sin(+\theta) \sin(+\phi), S \cos(\theta)) \quad (5)$$

$$S_j = (+S \sin(-\theta) \cos(+\phi), +S \sin(-\theta) \sin(+\phi), S \cos(\theta)) \quad (6)$$

$$S_k = (+S \sin(+\theta) \cos(-\phi), +S \sin(+\theta) \sin(-\phi), S \cos(\theta)) \quad (7)$$

where the notation for S_i , S_h , S_j and S_k was obtained following the notation in the literature⁷⁴. These equations define the new parameters θ and ϕ . Our definition of the polar and azimuthal angles differs from the direction of the Néel vectors presented in other works on anomalous transport⁷⁵. While the easy axis of the bulk SrRuO_3 is along the c-axis in the Pbnm notation, the staggered DMI induces spin canting along the a-axis and b-axis and creates four magnetic sublattices. From these equations, we can observe how all the subdominant components S_x and S_y are all different for a non-zero value of θ and ϕ , while the dominant component S_z is the same for all spins. Note that the set of equations (4-7) is valid for different magnetic phases with non-zero σ_{xy} , as described in the previous Section. The previous equations represent the magnetic configuration of the magnetic space group 62.448 in the BNS setting⁷⁶. We can obtain the ferromagnetic phase with spins along the z-axis for $\theta=\phi=0$,

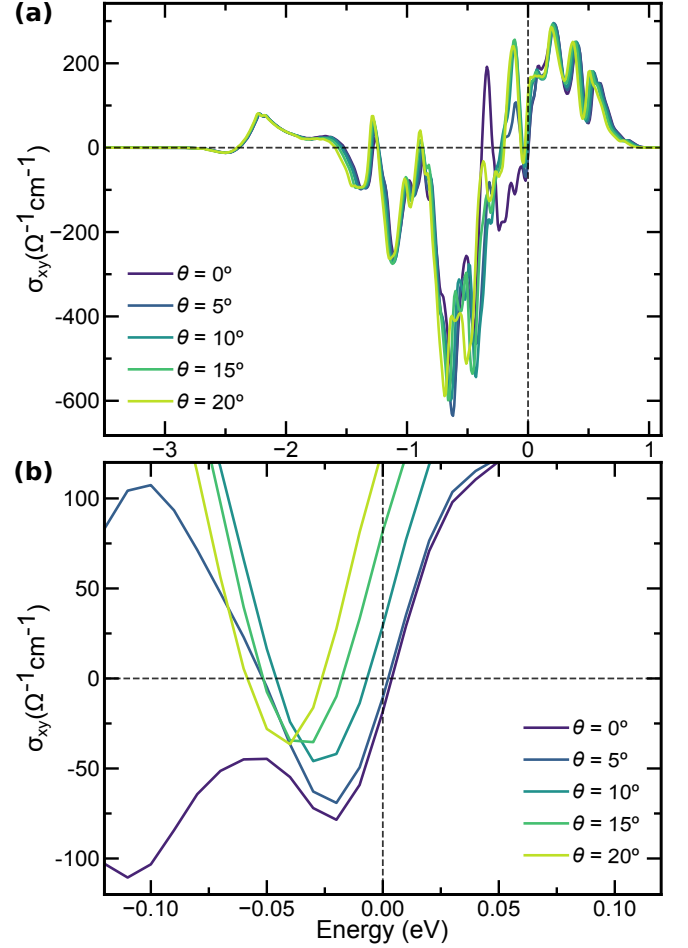


FIG. 10. (a) The sign change of the AHC at the Fermi level as a function of θ , keeping a constant value of ϕ at 0° . (b) Magnification along the energy window between -0.12 and 0.12 eV. The value of the spin-splitting is $\Delta=0.84$ eV.

G-type order with Néel vector along the x -axis for $\theta=\frac{\pi}{2}$ and $\phi=0$, and A-type order with Néel vector along the y -axis for $\theta=\frac{\pi}{2}$ and $\phi=\frac{\pi}{2}$. In the same way, the magnetic space group 62.448 represents the G-type order with spin component S_z and nonzero σ_{yz} . For the pure altermagnet, the staggered DMI contribution to the total energy does not bring any canting; therefore, we expect that it vanishes due to symmetry considerations. The analytical form of the staggered DMI for the ferromagnetic phase of SrRuO_3 will be given elsewhere⁷⁷. Both ferromagnetic and altermagnetic phases can be described by the same relativistic spin-momentum locking if they belong to the same magnetic space group. The only difference is that, in one case, the dominant component is s-wave, whereas in the second case, the dominant component is d-wave.⁴⁹

The evolution of S , θ , ϕ as functions of U is reported in Fig. 8. As observed in the DFT calculations in Fig. 8, the realistic ranges of the canting angles are 2° to 7° for θ and 5° to 33° for ϕ . The value of θ is always smaller than the value of ϕ . The Coulomb repulsion increases the magnetic moment, while it suppresses the spin-canting by

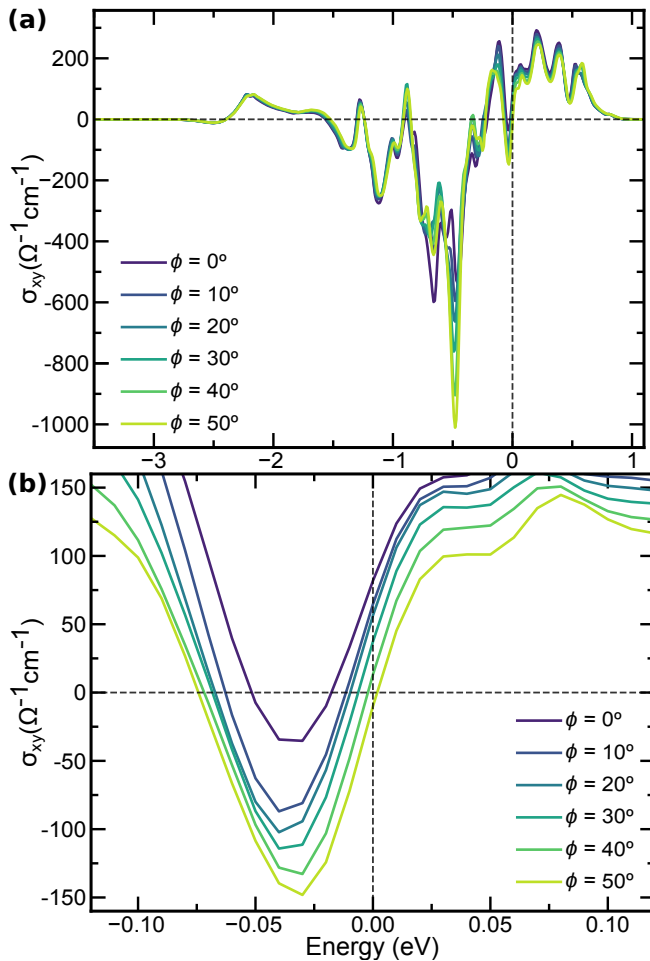


FIG. 11. (a) The sign change of the AHC at the Fermi level as a function of ϕ , keeping a constant value of θ at 15° . (b) Magnification along the energy window between -0.12 and 0.12 eV. The value of the spin-splitting is $\Delta=0.84$ eV.

pushing the spin-canting angles to lower values and more towards a collinear ferromagnet.

B. Sign change of the AHC due to spin canting

The spin cantings in the ferromagnetic phase induced by the DMI have been studied extensively in this section. The canting and azimuthal angles of the magnetic ground state have been varied across the entire parameter space, as shown in Fig. 9, for various values of spin splitting. Significant changes in the AHC at the Fermi level can be observed as the spin canting is varied. However, the variation of the AHC cannot be expressed as a simple function of the canting angles because of the numerically complicated formula of the AHC. Multiple sign changes can be observed throughout the parameter space.

Limiting ourselves to realistic values of θ and ϕ , we could observe sign changes in the AHC at the Fermi level corresponding to a spin-splitting of 0.84 eV. In Fig. 10,

we plot the AHC in the entire energy range between -3.5 eV and 1.1 eV and its magnification between -0.12 and +0.12 eV. A canting angle of 10° was sufficient to induce a sign change in the AHC at the Fermi level, as shown in Fig. 10. Similarly, corresponding to a canting angle of 15° , an azimuthal angle of 50° leads to the sign change as shown in Fig. 11. Therefore, not only the variation of the spin-splitting³⁰, but also the variation of the canting of the spin can induce a sign change in the AHC in SrRuO₃.

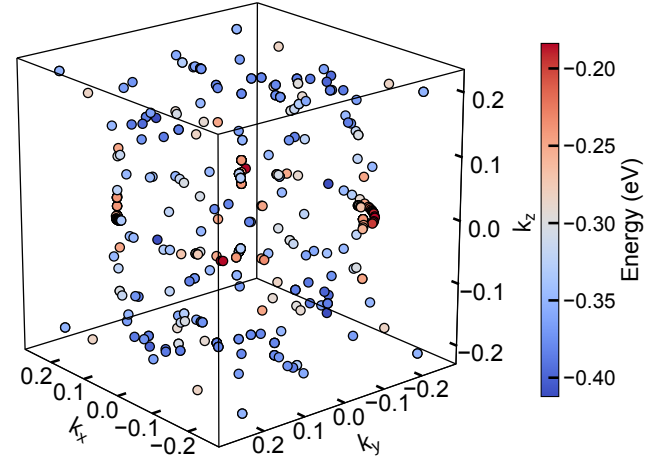


FIG. 12. The nodes of the system in reciprocal space plotted as a function of their energies with respect to the Fermi level. The values of the parameters are $\Delta=0.84$ eV, $\theta=\phi=0^\circ$. The system is ferromagnetic with magnetization oriented along the z -axis.

C. Evolution of the Weyl points due to spin canting

No Weyl points have been predicted or detected at the Fermi level, but it was proposed that Weyl points physics would dominate the spin dynamics of SrRuO₃⁷⁸. The variation of the AHC as a function of spin canting can be attributed to the evolution of the Weyl nodes induced by spin canting. To investigate this, we detect the Weyl nodes and analyze the trajectories of the Weyl points in momentum space as a function of θ and ϕ . The Weyl nodes of the ferromagnetic phase, characterized by a spin splitting of 0.84 eV, are shown in Fig. 12. Most of the Weyl points are located in the energy window between -0.4 and -0.2 eV, corresponding to region II defined in Fig. 3. We observe an extended distribution of several Weyl points, with a denser accumulation at $k_z=0$ along a circle-shaped curve.

The evolution of the Weyl nodes as a function of the canting angles θ and ϕ is presented in Figs. 13 and 14, respectively. We plot a limited region of the Brillouin zone to focus on the trajectory of a single Weyl node. The energy of the Weyl points varies by approximately 0.06 eV under changes in θ , whereas it changes by only about 0.01 eV under variations in ϕ , confirming that

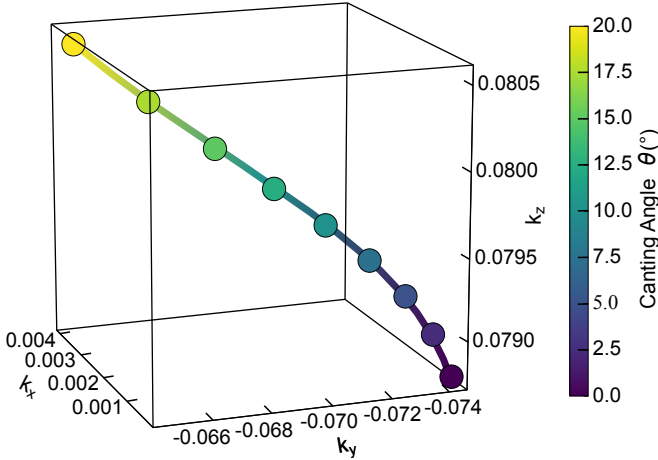


FIG. 13. Evolution of a Weyl point in the system as a function of θ , the other parameters are $\Delta=0.84$ eV and $\phi=0^\circ$. The energy of the Weyl point illustrated here is -0.35 eV. The canting induces a non-uniform variation in its energy, resulting in an energy range between -0.35 eV and -0.41 eV for the different values of θ . The trajectory of the Weyl point is plotted with a solid line.

the Weyl points and consequently, the AHC are more sensitive to the polar angle. In both cases, the nodes exhibit a non-linear dependence on the canting angles. All the Weyl nodes numerically extracted from the band structure evolve in a similar manner to those depicted in Figs. 13 and 14. Nevertheless, the trajectories traced by the Weyl nodes as the spin canting is varied are node dependent.

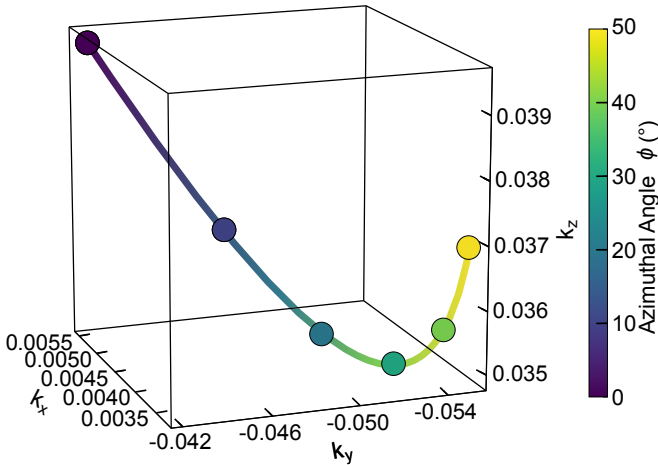


FIG. 14. Evolution of a Weyl point in the system as a function of ϕ for $\theta=15^\circ$ and $\Delta=0.84$ eV. The energy of the Weyl point illustrated here is -0.38 eV. The canting induces a non-uniform variation in its energy, resulting in an energy range between -0.378 eV and -0.386 eV for the different values of ϕ . The trajectory of the Weyl point is plotted with a solid line.

V. DISCUSSION AND CONCLUSIONS

We have introduced a simple and symmetry-preserving framework to compute the AHC as a function of spin-canting angles in ferromagnets and altermagnets. Starting from a nonmagnetic Hamiltonian obtained from first-principles calculations, magnetism is incorporated through on-site spin splitting, spin-orbit coupling, and controlled spin canting. Using the non-collinear ferromagnet SrRuO_3 as a representative system, we demonstrate that this approach captures both spin canting and the experimentally observed sign change of the AHC. We report the AHC for all directions of the spin for the ferromagnetic and altermagnetic phases. The magnetic transport properties are strongly anisotropic for all magnetic phases of SrRuO_3 . In the ferromagnetic phase of SrRuO_3 with magnetization along the z -axis, the low-energy AHC is found to be close to zero at the Fermi level, in agreement with experiments. The sensitivity of the AHC to the on-site spin splitting is shown to be maximal in the central region of the electronic bandwidth. We further identify the symmetry-allowed AHC tensor components for different magnetic orders in transition-metal perovskite ABO_3 compounds crystallizing in space group 62. For the ferromagnetic phase and for the C-type order with magnetization in the xy plane, both σ_{zx} and σ_{yz} are allowed. For the ferromagnetic phase with the dominant component in the xy plane, this is the spontaneous in-plane anomalous Hall effect and we tested through DFT calculations that the subdominant component produces a weak ferrimagnetism by spin canting. We also identify the symmetry relations between different components of the conductivity tensor.

Within DFT, we determine the range of spin-canting angles in SrRuO_3 and show that increasing electronic correlations suppresses canting. Our analysis of the AHC as a function of canting angles reveals that collinear magnetic configurations provide the dominant contribution to the AHC, while spin canting generally plays a secondary role in both ferromagnets and altermagnets. Nevertheless, canting can become significant when the collinear state exhibits an AHC close to zero, in which case it may induce a sign reversal. As a result, spin canting is one of the factors that must be taken into account when analyzing the sign change of the AHC in SrRuO_3 , and more generally in other compounds that allow spin canting. Finally, we track the evolution of Weyl points in the Brillouin zone as a function of the canting angle, elucidating their role in shaping the AHC. The Weyl points and the AHC are more sensitive to the variation of the polar angle.

The methodology introduced here can also be applied to more complex magnetic structures, such as those present in Kagome lattices, as well as to the investigation of topological systems and non-linear Hall effects. In these contexts, it offers a versatile framework for capturing the interplay between lattice geometry, electronic topology, and magnetic order, and may provide new in-

sights into emergent phenomena driven by Berry curvature and symmetry breaking.

ACKNOWLEDGMENTS

We acknowledge C. Ortix, R. Sattigeri, W. Brzezicki and M. Cuoco for useful discussions. This research was supported by the "MagTop" project (FENG.02.01-IP.05-0028/23) carried out within the "International Research Agendas" programme of the Foundation for Polish Science, co-financed by the European Union under the European Funds for Smart Economy 2021-2027 (FENG). C.A. and G.C. acknowledge support from PNRR MUR project PE0000023-NQSTI. We further acknowledge access to the computing facilities of the Interdisciplinary Center of Modeling at the University of Warsaw, Grants g91-1418, g91-1419, g96-1808, g96-1809, g103-2540, g104-2571, g104-2572 and g104-2573 for the availability of high-performance computing resources and support. We acknowledge the access to the computing facilities of the Poznan Supercomputing and Networking Center, Grants No. pl0267-01, pl0365-01, pl0471-01 and pl0694-01.

Appendix A: Computational details

First-principles calculations were performed using the Vienna Ab initio Simulation Package (VASP)^{79,80}, within the framework of density functional theory (DFT)

and employing the projector augmented-wave (PAW) method⁸¹. The exchange–correlation potential was described using the generalized gradient approximation (GGA) with the Perdew–Burke–Ernzerhof (PBE) functional⁸². A plane-wave cutoff energy of 400 eV was used, and the total energy convergence criterion was set to 10^{-6} eV. To account for electron-electron correlations among localized 4d orbitals, the DFT+ U formalism⁸³ was adopted to extract the range of the spin-canting angles. The Coulomb repulsion was tuned from 0 to 3 eV, which is a reasonable range for the 4d Ru atoms^{40–42}.

SrRuO_3 crystallizes in an orthorhombic structure with space group $Pbnm$ (No. 62). The experimental lattice constants of SrRuO_3 in $Pbnm$ notation are $a=5.5670 \text{ \AA}$, $b=5.5304 \text{ \AA}$ and $c=7.8446 \text{ \AA}$, and in $Pnma$ they are $a=5.5304 \text{ \AA}$, $b=7.8446 \text{ \AA}$ and $c=5.5670 \text{ \AA}$. An effective Hubbard parameter of $U = 3 \text{ eV}$ was employed, with Hund's exchange coupling set to $J_H = 0.15U$. A Monkhorst–Pack k -point grid of $10 \times 10 \times 7$ was used for spin-resolved band-structure calculations.

To extract the non-magnetic Hamiltonian, we utilize the WANNIER90 software, which transforms Bloch states into Wannier states^{84,85}. The AHC was calculated by utilising WannierTools⁸⁶. A $101 \times 101 \times 101$ k -point grid was used to perform these calculations on the Wannier Hamiltonian: convergence tests were performed with $201 \times 201 \times 201$ k -point grid, but minor changes were observed in the conductivity. The Weyl point positions were obtained by applying the node-finding routine provided in WannierTools.

* mbenny@magtop.ifpan.edu.pl

† jskolimowski@magtop.ifpan.edu.pl

‡ autieri@magtop.ifpan.edu.pl

¹ A. P. Petrović, C. Psaroudaki, P. Fischer, M. Garst, and C. Panagopoulos, *Rev. Mod. Phys.* **97**, 031001 (2025).

² A. N. Bogdanov and C. Panagopoulos, *Nature Reviews Physics* **2**, 492–498 (2020).

³ S. K. Jena, R. Islam, E. Milińska, M. M. Jakubowski, R. Minikayev, S. Lewińska, A. Lynnyk, A. Pietruczik, P. Aleszkiewicz, C. Autieri, and A. Wawro, *Nanoscale* **13**, 7685–7693 (2021).

⁴ J. Guo, X. Zeng, and M. Yan, *Physical Review B* **96**, 014404 (2017).

⁵ M. Roig, Y. Yu, R. C. Ekman, A. Kreisel, B. M. Andersen, and D. F. Agterberg, *Phys. Rev. Lett.* **135**, 016703 (2025).

⁶ C. Autieri, R. M. Sattigeri, G. Cuono, and A. Fakhredine, *Phys. Rev. B* **111**, 054442 (2025).

⁷ L. Šmejkal, J. Sinova, and T. Jungwirth, *Phys. Rev. X* **12**, 031042 (2022).

⁸ L. Šmejkal, J. Sinova, and T. Jungwirth, *Phys. Rev. X* **12**, 040501 (2022).

⁹ P. A. McClarty and J. G. Rau, *Phys. Rev. Lett.* **132**, 176702 (2024).

¹⁰ L. Šmejkal, R. González-Hernández, T. Jungwirth, and J. Sinova, *Science Advances* **6**, eaaz8809 (2020),

<https://www.science.org/doi/pdf/10.1126/sciadv.aaz8809>.

¹¹ R. D. Gonzalez Betancourt, J. Zubáč, R. Gonzalez-Hernandez, K. Geishendorf, Z. Šobáň, G. Springholz, K. Olejník, L. Šmejkal, J. Sinova, T. Jungwirth, S. T. B. Goennenwein, A. Thomas, H. Reichlová, J. Železný, and D. Kriegner, *Phys. Rev. Lett.* **130**, 036702 (2023).

¹² A. J. Wu, B. Z. Zhang, C. J. Liu, and D. X. Shao, *Applied Physics Letters* **123**, 052407 (2023).

¹³ I. Turek, *Physical Review B* **106**, 094432 (2022).

¹⁴ D.-F. Shao, Y.-Y. Jiang, J. Ding, S.-H. Zhang, Z.-A. Wang, R.-C. Xiao, G. Gurung, W. Lu, Y. Sun, and E. Y. Tsymbal, *Physical Review Letters* **130**, 216702 (2023).

¹⁵ D.-F. Shao, S.-H. Zhang, G. Gurung, W. Yang, and E. Y. Tsymbal, *Phys. Rev. Lett.* **124**, 067203 (2020).

¹⁶ Y. Fang, J. Cano, and S. A. A. Ghorashi, *Physical Review Letters* **133** (2024), 10.1103/physrevlett.133.106701.

¹⁷ E. Derunova, J. Gayles, Y. Sun, M. W. Gaulois, and M. N. Ali, *SciPost Physics Core* **8** (2025), 10.21468/scipostphyscore.8.4.085.

¹⁸ Z. Liu, M. Wei, W. Peng, D. Hou, Y. Gao, and Q. Niu, *Phys. Rev. X* **15**, 031006 (2025).

¹⁹ R.-C. Xiao, Y. Jin, Z.-F. Zhang, Z.-H. Feng, D.-F. Shao, and M. Tian, *Computer Physics Communications* , 109872 (2025).

²⁰ M. dos Santos Dias, N. Biniskos, F. J. dos Santos,

K. Schmalzl, J. Persson, F. Bourdarot, N. Marzari, S. Blügel, T. Brückel, and S. Lounis, *Nature Communications* **14** (2023), 10.1038/s41467-023-43042-3.

²¹ C. Autieri and A. Fakhredine, *The Journal of Physical Chemistry Letters* **17**, 449 (2026), pMID: 41469325.

²² C. Autieri, G. Cuono, D. Chakraborty, P. Gentile, and A. M. Black-Schaffer, *Phys. Rev. B* **112**, 014412 (2025).

²³ A. León, C. Autieri, T. Brumme, and J. W. González, *npj Quantum Materials* **10** (2025), 10.1038/s41535-025-00814-y.

²⁴ T. P. T. Nguyen and K. Yamauchi, *Phys. Rev. B* **107**, 155126 (2023).

²⁵ G. Cuono, R. M. Sattigeri, J. Skolimowski, and C. Autieri, *Journal of Magnetism and Magnetic Materials* **586**, 171163 (2023).

²⁶ F. Bernardini, M. Fiebig, and A. Cano, *Journal of Applied Physics* **137**, 103903 (2025).

²⁷ M. Kim and B. I. Min, *Phys. Rev. B* **91**, 205116 (2015).

²⁸ G. Koster, L. Klein, W. Siemons, G. Rijnders, J. S. Dodge, C.-B. Eom, D. H. A. Blank, and M. R. Beasley, *Rev. Mod. Phys.* **84**, 253 (2012).

²⁹ T. C. van Thiel, W. Brzezicki, C. Autieri, J. R. Hortensius, D. Afanasiev, N. Gauquelin, D. Jannis, N. Janssen, D. J. Groenendijk, J. Fatemans, S. Van Aert, J. Verbeeck, M. Cuoco, and A. D. Caviglia, *Phys. Rev. Lett.* **127**, 127202 (2021).

³⁰ D. J. Groenendijk, C. Autieri, T. C. van Thiel, W. Brzezicki, J. R. Hortensius, D. Afanasiev, N. Gauquelin, P. Barone, K. H. W. van den Bos, S. van Aert, J. Verbeeck, A. Filippetti, S. Picozzi, M. Cuoco, and A. D. Caviglia, *Phys. Rev. Res.* **2**, 023404 (2020).

³¹ G. Malsch, D. Ivaneyko, P. Milde, L. Wysocki, L. Yang, P. H. M. van Loosdrecht, I. Lindfors-Vrejoiu, and L. M. Eng, *ACS Applied Nano Materials* **3**, 1182 (2020).

³² Z. Lu, J. Feng, X. Zheng, Y. guo Shi, R.-W. Li, C. Autieri, M. Cuoco, M. Radovic, and Z. Wang, “Insulator-to-metal transition via magnetic reconstruction at oxide interfaces,” (2025), arXiv:2503.21093 [cond-mat.mes-hall].

³³ Z. Li, X. Chen, Y. Chen, Q. Zhang, H. Zhang, J. Zhang, W. Shi, B. He, J. Zhang, J. Song, F. Han, B. Liu, L. Gu, F. Hu, Y. Chen, B. Shen, and J. Sun, *Mater. Horiz.* **8**, 3468 (2021).

³⁴ G. Kimbell, C. Kim, W. Wu, M. Cuoco, and J. W. A. Robinson, *Communications Materials* **3** (2022), 10.1038/s43246-022-00238-2.

³⁵ M. Cuoco and A. Di Bernardo, *APL Materials* **10**, 090902 (2022).

³⁶ Z. Lu, Y. Yang, L. Wen, J. Feng, B. Lao, X. Zheng, S. Li, K. Zhao, B. Cao, Z. Ren, D. Song, H. Du, Y. Guo, Z. Zhong, X. Hao, Z. Wang, and R.-W. Li, *npj Flexible Electronics* **6** (2022), 10.1038/s41528-022-00141-3.

³⁷ L. Gao, Y. Wang, X. Lyu, P. Liu, M. Zhu, J. Liu, M. Li, A. Ji, Q. Zhang, L. Gu, L. Ma, Z. Cao, and N. Lu, *Advanced Science* **n/a**, e22085 (2026).

³⁸ A. T. Zayak, X. Huang, J. B. Neaton, and K. M. Rabe, *Phys. Rev. B* **77**, 214410 (2008).

³⁹ D. Tian, Z. Liu, S. Shen, Z. Li, Y. Zhou, H. Liu, H. Chen, and P. Yu, *Proceedings of the National Academy of Sciences* **118** (2021), 10.1073/pnas.2101946118.

⁴⁰ O. Gränäs, I. Di Marco, O. Eriksson, L. Nordström, and C. Etz, *Phys. Rev. B* **90**, 165130 (2014).

⁴¹ K. Gupta, B. Mandal, and P. Mahadevan, *Phys. Rev. B* **90**, 125109 (2014).

⁴² C. Autieri, *Journal of Physics: Condensed Matter* **28**, 426004 (2016).

⁴³ A. Huang, H.-T. Jeng, and C.-H. Chang, *ACS Applied Nano Materials* **4**, 5932–5939 (2021).

⁴⁴ C. Piamonteze, F. Bern, S. R. V. Avula, M. Studniarek, C. Autieri, M. Ziese, and I. Lindfors-Vrejoiu, *Applied Physics Letters* **118**, 152408 (2021).

⁴⁵ N. Filipoiu, N. Plugaru, T. Sandu, R. Plugaru, and G. Alexandru Nemnes, *Nanotechnology* **36**, 075702 (2024).

⁴⁶ S. Peng, X. Zheng, S. Li, B. Lao, Y. Han, Z. Liao, H. Zheng, Y. Yang, T. Yu, P. Liu, Y. Sun, X.-Q. Chen, S. Peng, W. Zhao, R.-W. Li, and Z. Wang, *Nature Materials* **24**, 1749–1755 (2025).

⁴⁷ K.-H. Ahn, A. Marmodoro, J. Hejtmánek, Z. Jirák, and K. Knížek, *Phys. Rev. B* **105**, 245107 (2022).

⁴⁸ J. Kipp, K. Samanta, F. R. Lux, M. Merte, D. Go, J.-P. Hanke, M. Redies, F. Freimuth, S. Blügel, M. Ležaić, and Y. Mokrousov, *Communications Physics* **4**, 99 (2021).

⁴⁹ X. Gong, A. Fakhredine, and C. Autieri, Submitted (2026).

⁵⁰ S. Nishihaya, Y. Matsuki, H. Kaminakamura, H. Sugeno, M. Jiang, Y. Murakami, R. Arita, H. Ishizuka, and M. Uchida, *Advanced Materials* **37** (2025), 10.1002/adma.202502624.

⁵¹ W. Brzezicki, C. Autieri, and M. Cuoco, *Advanced Electronic Materials* **11** (2025), 10.1002/aelm.202500307.

⁵² H. Chen, Y. Jin, M. Yahyavi, I. Belopolski, S. Shao, T. Hou, N. Wang, C.-H. Hsu, Y. Zhao, B. Yang, Q. Ma, J.-X. Yin, S.-Y. Xu, W.-b. Gao, and G. Chang, *Phys. Rev. B* **109**, 125305 (2024).

⁵³ X. Wang, J. R. Yates, I. Souza, and D. Vanderbilt, *Physical Review B* **74**, 195118 (2006).

⁵⁴ C. Chen Ye, K. Tenzin, J. Ślawińska, and C. Autieri, *Phys. Rev. B* **113**, 014413 (2026).

⁵⁵ J. Skolimowski, C. Autieri, K. Jamrosczyk, and M. Benny, “Soc_code_v1,” https://github.com/jskol/SOC_Code_V1 (2025), accessed: 2025-11-11.

⁵⁶ M.-W. Yoo and A. Hoffmann, “Micromagnetic formalism for magnetic multipoles,” (2025), arXiv:2501.07513 [cond-mat.mes-hall].

⁵⁷ S.-W. Cheong and F.-T. Huang, *npj Quantum Materials* **9**, 13 (2024).

⁵⁸ B. Singh, H. Lin, and A. Bansil, *Advanced Materials* **35**, 2201058 (2023).

⁵⁹ W. Brzezicki, *Journal of Physics: Condensed Matter* **32**, 023001 (2019).

⁶⁰ K. Singh, J. Skolimowski, G. Cuono, R. M. Sattigeri, A. Ptok, O. Pavloviuk, T. Romanova, T. Toliński, P. Wiśniewski, C. Autieri, and D. Kaczorowski, *Phys. Rev. B* **112**, 134440 (2025).

⁶¹ A. Tamai, M. Zingl, E. Rozbicki, E. Cappelli, S. Riccò, A. de la Torre, S. McKeown Walker, F. Y. Bruno, P. D. C. King, W. Meevasana, M. Shi, M. Radović, N. C. Plumb, A. S. Gibbs, A. P. Mackenzie, C. Berthod, H. U. R. Strand, M. Kim, A. Georges, and F. Baumberger, *Phys. Rev. X* **9** (2019).

⁶² L.-D. Yuan and A. Zunger, *Advanced Materials* , 2211966 (2023).

⁶³ J. Zhong, J. Zhuang, and Y. Du, *Chinese Physics B* **32**, 047203 (2023).

⁶⁴ J. Yu, Z. Li, Z. Guo, S. Qian, X. Wang, and Z. Liu, *Advanced Electronic Materials* **11**, e00714 (2025).

⁶⁵ M. Ziese and I. Vrejoiu, *Phys. Rev. B* **84**, 104413 (2011).

⁶⁶ M. Ezawa, *Phys. Rev. B* **112**, 235307 (2025).

⁶⁷ R. González-Hernández, L. Šmejkal, K. Výborný, Y. Ya-

hagi, J. Sinova, T. c. v. Jungwirth, and J. Železný, Phys. Rev. Lett. **126**, 127701 (2021).

⁶⁸ N. Nagaosa, J. Sinova, S. Onoda, A. H. MacDonald, and N. P. Ong, Rev. Mod. Phys. **82**, 1539 (2010).

⁶⁹ A. Fakhredine, G. Cuono, J. Skolimowski, S. Picozzi, and C. Autieri, In preparation (2026).

⁷⁰ K. Samanta, M. Ležaić, M. Merte, F. Freimuth, S. Blügel, and Y. Mokrousov, J. Appl. Phys. **127**, 213904 (2020).

⁷¹ M. Daghofer, K. Wohlfeld, and J. van den Brink, “Alter-magnetic polarons: the fate of alter magnetic band splittings at strong coupling,” (2025), arXiv:2506.03261 [cond-mat.str-el].

⁷² Y. Guo, H. Liu, O. Janson, I. C. Fulga, J. van den Brink, and J. I. Facio, Materials Today Physics **32**, 100991 (2023).

⁷³ T. Moriya, Phys. Rev. **120**, 91 (1960).

⁷⁴ C. Weingart, N. Spaldin, and E. Bousquet, Phys. Rev. B **86**, 094413 (2012).

⁷⁵ M. Dou, X. Wang, and L. L. Tao, Phys. Rev. B **111**, 224423 (2025).

⁷⁶ M. I. Aroyo, J. M. Perez-Mato, C. Capillas, E. Kroumova, S. Ivantchev, G. Madariaga, A. Kirov, and H. Wondratschek, Zeitschrift für Kristallographie - Crystalline Materials **221**, 15–27 (2006).

⁷⁷ M. Benny, X. Gong, A. Fakhredine, and C. Autieri, In manuscript (2026).

⁷⁸ S. Itoh, Y. Endoh, T. Yokoo, S. Ibuka, J.-G. Park, Y. Kaneko, K. S. Takahashi, Y. Tokura, and N. Nagaosa, Nature Communications **7** (2016), 10.1038/ncomms11788.

⁷⁹ G. Kresse and J. Hafner, Physical review B **47**, 558 (1993).

⁸⁰ G. Kresse and J. Furthmüller, Computational materials science **6**, 15 (1996).

⁸¹ G. Kresse and D. Joubert, Physical review b **59**, 1758 (1999).

⁸² J. P. Perdew, K. Burke, and M. Ernzerhof, Physical review letters **77**, 3865 (1996).

⁸³ A. Liechtenstein, V. I. Anisimov, and J. Zaanen, Physical Review B **52**, R5467 (1995).

⁸⁴ A. A. Mostofi, J. R. Yates, Y. S. Lee, I. Souza, D. Vanderbilt, and N. Marzari, Comput. Phys. Comm. **178**, 685 (2008).

⁸⁵ A. A. Mostofi, J. R. Yates, G. Pizzi, Y.-S. Lee, I. Souza, D. Vanderbilt, and N. Marzari, Computer Physics Communications **185**, 2309 (2014).

⁸⁶ Q. Wu, S. Zhang, H.-F. Song, M. Troyer, and A. A. Soluyanov, Computer Physics Communications **224**, 405 (2018).